ACS APPLIED MATERIALS & INTERFACES
www.acsami.org
Research Article

Surface Hexagonal Pt_1Sn_1 Intermetallic on Pt Nanoparticles for Selective Propane Dehydrogenation

Chenliang Ye,[‖] Mao Peng,[‖] Yunhao Wang, Ningqiang Zhang, Dingsheng Wang, Miaolun Jiao,* and Jeffrey T. Miller*

Cite This: ACS Appl. Mater. Interfaces 2020, 12, 25903−25909
Read Online
ACCESS | Metrics & More | Article Recommendations | Supporting Information

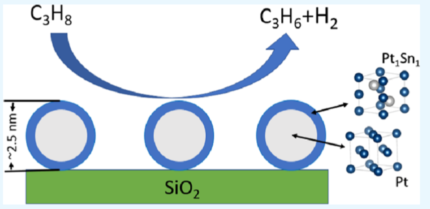

ABSTRACT: A series of 2−3 nm Pt−Sn bimetallic nanoparticles with different Pt−Sn coordination numbers were synthesized by a stepwise approach including electrostatic adsorption and temperature-programmed reduction of metal precursors on the SiO_2 support. In situ synchrotron X-ray diffraction (XRD) and X-ray absorption fine structure (XAFS) demonstrated a highly ordered hexagonal Pt_1Sn_1 intermetallic shell on Pt nanoparticles. The turnover rates (TORs), propylene selectivity, and stability of these bimetallic catalysts significantly surpass those of the monometallic Pt catalyst for propane dehydrogenation. At the same time, TORs increase with increasing the Pt−Sn coordination number, whereas propylene selectivity is not significantly influenced by the Pt−Sn coordination number. Combined with experiments and theoretical calculations, the high propylene selectivity of Pt−Sn bimetallic nanoparticles is attributed to the geometric effects of Sn that reduce the Pt ensembles, and the high TORs are due to the electronic effects that weaken Pt−hydrocarbon chemisorption energies.

KEYWORDS: *Pt−Sn bimetallic nanoparticles, intermetallic, propane dehydrogenation, geometric structure, electronic structure*

1. INTRODUCTION

Nanoalloys have attracted great attentions in heterogeneous catalysis due to their high ratio of surface atoms and potential for improving catalytic performance by modifying the geometric and electronic structure of active metals.[1−5] Typically, alloys are classified into two categories according to the atomic order: solid solutions and intermetallic compounds.[6] Solid solutions often contain metals of similar atomic size and electronic character identical to that of the parent metal with random atomic arrangements. By contrast, intermetallic compounds possess a uniform crystal structure and highly ordered atomic arrangements. In several cases, nanoparticles include two phases with an intermetallic shell on a pure phase noble metal core.[7−9] It is challenging to precisely identify the structure of nanoalloys with small particle sizes, especially under realistic reaction conditions.[10]

With the surge of shale gas, light alkane dehydrogenation becomes increasingly important to synthesize olefins.[11] Pt catalysts are the most widely applied materials for light alkane dehydrogenation.[12] Compared with monometallic Pt, bimetallic nanoalloys, such as Pt−Sn, Pt−Zn, Pt−In, Pt−Ga, Pt−Cu, and Pt−Sb, exhibit improved catalytic performance with Pt−Sn alloys being the most successful example.[13−20] Both geometric and electronic effects have been suggested to explain the improved catalytic performance. Geometric effects in Pt−Sn alloys, for example, reduce the Pt ensemble size, decrease the hydrogenolysis rate, and increase olefin selectivity.[21,22] Electronic effects are thought to weaken adsorbate bond energies, enhance desorption of surface-bounded olefin, and limit its further dehydrogenation, resulting in higher olefin selectivity, reaction rates, and improved lifetime.[12,23] However, due to the challenges of characterizing and controlling the catalytic surface structure, the intrinsic contribution of Sn on Pt for light alkane dehydrogenation is still under debate.

Herein, we synthesized a series of SiO_2-supported Pt@Pt_1Sn_1 nanoparticles with a highly ordered hexagonal Pt_1Sn_1 intermetallic shell (structure type NiAs) on Pt nanoparticles for propane dehydrogenation. The structure of the surface Pt_1Sn_1 is stable at 550 °C, and the Pt−Sn coordination number is controllable by varying Sn loadings. The turnover rates (TORs), propylene selectivity, and stability of these bimetallic catalysts for propane dehydrogenation significantly surpass those of the monometallic Pt. At the same time, TORs increase with increasing Pt−Sn coordination number, whereas propylene selectivity is not significantly influenced by the Pt−Sn coordination number. Combined with experiments and theoretical calculations, we suggest that the high propylene selectivity of the Pt−Sn bimetallic nanoparticles is attributed to the geometric effects of Sn that reduce the Pt ensembles, and

Received: March 17, 2020
Accepted: May 19, 2020
Published: May 19, 2020

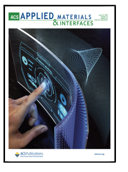

the high TORs are due to the electronic effects that weaken Pt−hydrocarbon chemisorption energies.

2. EXPERIMENTAL SECTION

2.1. Synthesis of Catalysts. The Pt−Sn bimetallic catalysts of a target Pt loading of 2 wt % were synthesized with different Sn loadings. Various amounts of $SnCl_4$ were dissolved in 4.0 mL of methanol and added dropwise to 5.3 g silica. The obtained Sn/SiO_2 was dried overnight at 125 °C and calcined at 550 °C for 3 h. $Pt(NH_3)_4(NO_3)_2$ (0.21 g) was dissolved in 3.5 mL of water, and ammonium hydroxide solution was added to the solution until the pH reached 11. The solution was added dropwise to the obtained Sn/SiO_2. This catalyst was then dried overnight at 125 °C and calcined at 225 °C for 3 h. Finally, the catalyst was reduced in 5% H_2/N_2 (150 mL/min) at 150° for 10 min, 200° for 30 min, 250° for 10 min, and 550° for 30 min. The sample is named as $xSnPt/SiO_2$, where x denotes the mass loading of Sn. For comparison, Sn/SiO_2 and Pt/SiO_2 catalysts with 2 wt % Pt/Sn loading were also prepared using the same method.

2.2. Characterization. Scanning transmission electron microscope (STEM) experiments for determining particle size were conducted using the FEI Titan scanning transmission electron microscope (80−300 kV, 1 nm spatial resolution) with a high angle annular dark-field (HAADF) detector at 300 kV at Birck Nanotechnology Center, Purdue University. The particle size distribution was determined by counting 200 particles for each sample using Nano Measurer 1.2. The in situ synchrotron XRD experiment was performed at the 11-ID-C beamline at the APS, Argonne National Lab. Diffraction data was acquired in the transmission mode with a PerkinElmer large area detector using X-rays at 105.715 keV (λ = 0.11730 Å). X-ray absorption measurements with a transmission mode were acquired on the bending magnet beamline of the Materials Research Collaborative Access Team (MRCAT) at the Advanced Photon Source, Argonne National Laboratory. Pt dispersion was determined by CO chemisorption using Micromeritics ASAP 2020 chemisorption equipment. Pt dispersion was calculated by assuming a stoichiometry of CO:Pt = 1.

2.3. Catalytic Testing. Propane dehydrogenation was tested in a fixed-bed quartz tube reactor with an internal diameter of 9.5 mm. The reaction temperature was monitored by an internal thermocouple placed at the center of the catalyst bed. The products were analyzed by a gas chromatograph with a flame ionization detector (FID). Before each test, the catalyst was reduced at 550 °C for 30 min with 5% H_2/N_2 (50 mL/min). The reaction temperature was 500 °C, and the reactants were 2% C_3H_8, 3% H_2, and balanced N_2. The gas hourly space velocity (GHSV) was adjusted to determine the selectivity at certain conversions. The turnover rates (TORs) were calculated from the moles of propylene produced per surface Pt site determined by Pt dispersions. For the stability test, the weight of samples was fixed at 0.02 g, and the flow rates were 150 mL/min.

2.4. Theoretical Calculations. All calculations have been performed in the framework of density functional theory (DFT) implemented by the $Dmol^3$ program package in Materials Studio; exchange−correlation effects are described with the generalized gradient approximation (GGA) using the Perdew−Burke−Ernzerhof (PBE) functional. A 3 × 3 × 1 Monkhorst−Pack *k*-point grid is used for the integrations of the Brillouin zone. The double-numerical basis set with a polarization d-function (DNP) is chosen to expand the valence electron functions. We used Pt(111) (the most stable low exponential surface) to imitate the Pt nanoparticle; Pt(111) was modeled by a $p(3 \times 3)$ super cell with four layers, and the top three layers containing an adsorbate are relaxed. $Pt_1Sn_1(110)$ means Pt_1Sn_1 full-body intermetallic, and $Pt_1Sn_1(110)$ was modeled by a $p(2 \times 2)$ super cell and contained three layers, in which the top two layers are allowed to relax. $Pt_1Sn_1(110)/Pt(111)$ was considered a Pt_1Sn_1 shell on top of Pt with a single layer of Pt_1Sn_1. The vacuum region was set 15 Å to avoid interperiodic interaction. Surface energy is determined by $\gamma = (E_{slab} - NE_{bulk})/2A$, where E_{slab} and E_{bulk} are the total energies of the slab and one bulk unit cell, respectively, N is the number of bulk units in the slab, and A is the surface area of the slab. The adsorption energy of surface species is defined as $E_{ads} = E_{adsorbate/slab} - E_{slab} - E_{adsorbate}$, where $E_{adsorbate/slab}$, $E_{adsorbate}$, and E_{slab} are the calculated total energies of a surface slab with the species, gaseous-phase molecule, and the clean surface, respectively.

3. RESULTS AND DISCUSSION

The Pt−Sn bimetallic catalysts with different Sn loadings were synthesized through a stepwise approach including electrostatic adsorption and temperature-programmed reduction of metal precursors on the SiO_2 support. First, tin chloride and tetraamine platinum(II) nitrate were sequentially impregnated on SiO_2. The tetraamine platinum(II) nitrate solution is sufficiently basified to adsorb $[Pt(NH_3)_4]^{2+}$on the SiO_2 surface, which induces strong electrostatic adsorption of positively charged $[Pt(NH_3)_4]^{2+}$ to the deprotonated silica surface.[24] Then, the $Pt-Sn/SiO_2$ precursors were reduced at around 200 °C to obtain metallic Pt, followed by reduction at a higher temperature to form a Pt−Sn bimetallic phase on the Pt surface. As shown in Figures 1 and S1, the average particle sizes

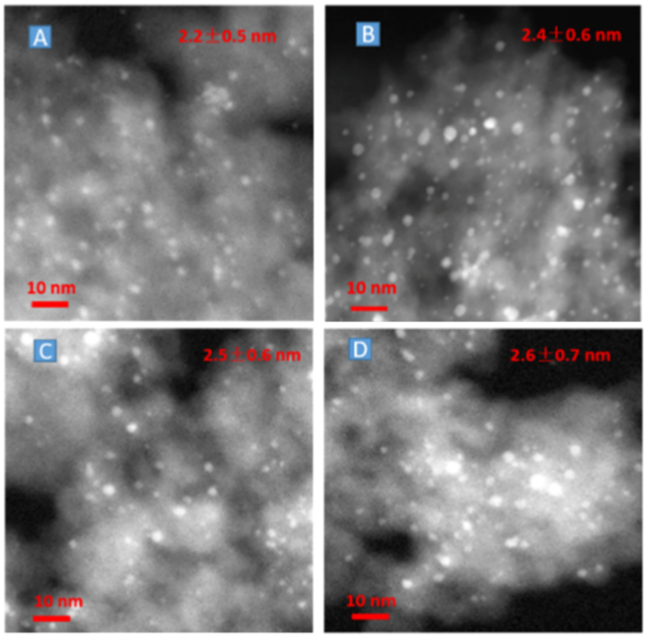

Figure 1. STEM image of the samples: (A) Pt/SiO_2, (B) $1SnPt/SiO_2$, (C) $4SnPt/SiO_2$, and (D) $8SnPt/SiO_2$.

of the Pt and Pt−Sn bimetallic catalysts are around 2−3 nm. The uniform particle sizes of these samples result from the strong electrostatic adsorption of the Pt precursors to the support, which allows comparing their catalytic kinetics at the same particle sizes. In situ synchrotron XRD with a high energy (105.715 keV) was employed to determine the long-range-order structure of the catalysts. The synchrotron X-ray provides enough signal intensity and resolution to identify diffraction peaks of 2−3 nm nanoparticles, while the high energy leads to lower-angle diffraction peaks according to Bragg's law ($2d \sin\theta = n\lambda$).[25] As displayed in Figure 2A, with background subtracted, the Pt/SiO_2 catalyst shows four diffraction peaks at 2θ of 2.98, 3.43, 4.88, and 5.71°, corresponding to (111), (200), (220), and (311) of face-centered cubic (FCC) Pt. At a low Sn loading, the diffraction spectrum of the $1SnPt/SiO_2$ sample is similar to that of Pt/SiO_2. With increasing Sn loadings, new diffraction peaks at 2θ

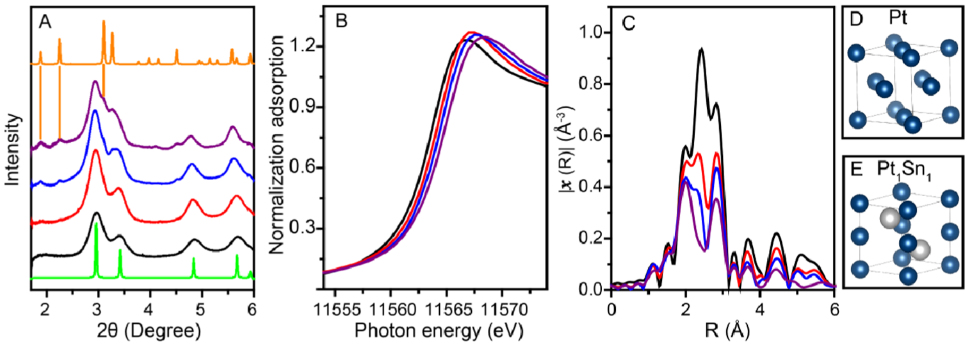

Figure 2. In situ XRD, X-ray absorption fine structure (XAFS), and crystal structure of the samples: (A) XRD of Pt/SiO_2 (black), $1SnPt/SiO_2$ (red), $4SnPt/SiO_2$ (blue), $8SnPt/SiO_2$ (purple), Pt simulation (green), and Pt_1Sn_1 simulation (orange). (B) X-ray absorption near-edge spectroscopy (XANES) of Pt/SiO_2 (black), $1SnPt/SiO_2$ (red), $4SnPt/SiO_2$ (blue), and $8SnPt/SiO_2$ (purple). (C) k^2-weighted R-space extended XAFS (EXAFS) of Pt/SiO_2 (black), $1SnPt/SiO_2$ (red), $4SnPt/SiO_2$ (blue), and $8SnPt/SiO_2$ (purple). (D) Pt of the FCC structure. (E) Pt_1Sn_1 of the NiAs structure.

Table 1. R-Space EXAFS Fitting Results of the Samples[a]

sample	scattering path	distance (Å)	C.N.	σ^2 ($Å^2$)	ΔE_0 (eV)	R-factor
Pt/SiO_2	Pt−Pt	2.74 ± 0.01	9.7 ± 0.5	0.007 ± 0.001	6.9 ± 0.4	0.003
$1SnPt/SiO_2$	Pt−Pt	2.74 ± 0.01	8.5 ± 0.6	0.008 ± 0.001	2.5 ± 0.9	0.001
	Pt−Sn	2.64 ± 0.02	0.8 ± 0.4	0.007 ± 0.003	2.5 ± 0.9	
$4SnPt/SiO_2$	Pt−Pt	2.74 ± 0.01	7.4 ± 0.9	0.009 ± 0.001	2.0 ± 1.3	0.003
	Pt−Sn	2.66 ± 0.03	2.0 ± 0.8	0.013 ± 0.004	2.0 ± 1.3	
$8SnPt/SiO_2$	Pt−Pt	2.76 ± 0.01	5.6 ± 0.9	0.010 ± 0.002	2.4 ± 1.0	0.003
	Pt−Sn	2.67 ± 0.01	3.7 ± 0.5	0.013 ± 0.002	2.4 ± 1.0	

[a]Fittings were done using k^2-weighted R-space EXAFS spectra with the k-range of 3.0−12.0 $Å^{-1}$ and the R range of 1.7−3.2 Å. The amplitude reduction factor is 0.75 based on the fitting of Pt foil.

of 1.89 and 2.25° are observed in $4SnPt/SiO_2$ and $8SnPt/SiO_2$, respectively, which corresponds to a highly ordered hexagonal Pt_1Sn_1 intermetallic compound. XRD results confirm the formation of two phases of Pt−Sn bimetallic catalysts, which are metallic Pt and Pt_1Sn_1 intermetallic compounds (structure type NiAs). Notably, even though the Sn loadings reach 8%, SnO_x is not observed in XRD, which could be attributed to the well dispersion or lack of the long-range-order structure of SnO_x.

In situ Pt L_3 edge XAFS measurements were conducted to investigate the local structure of Pt. As shown in Figure 2B, the Pt L_3 edge energy of Pt/SiO_2 is 11 564 eV, which is identical to that of metallic Pt. The XANES energy shifts to a higher level with increasing Sn loadings, suggesting a higher energy level of unfilled Pt 5d states. The Fourier transform k^2-weighted R-space EXAFS of a monometallic Pt catalyst shows three main peaks between 1.7 and 3.2 Å, and the peak positions and Fourier transform magnitudes continue to change with increasing Sn loading, indicating scattering from metallic Sn and changes in bond distance and coordination numbers (Figure 2C). Table 1 lists the R-space EXAFS fitting results (Figures S2 and S3 display the fitting spectra). The Pt−Pt coordination number of Pt/SiO_2 is 9.4, indicating typical 2−3 nm Pt nanoparticles, which agrees with the STEM results. For $1SnPt/SiO_2$, the Pt−Sn coordination number is only 0.8, and there are excessive Pt−Pt bonds, suggesting a Pt-rich bimetallic nanoparticle, which leads to the similar XRD spectra between $1SnPt/SiO_2$ and Pt/SiO_2. With increasing Sn loadings, the Pt−Sn coordination number continues to increase, suggesting a higher ratio of Pt_1Sn_1 in the Pt−Sn bimetallic catalysts. The Pt−Sn bond distance (2.73 Å) is close to the Pt−Pt bond distance (2.72 Å) in the typical Pt_1Sn_1 intermetallic (ISCD 42593). However, in our bimetallic samples, the Pt−Sn bond distance is significantly shorter than the Pt−Pt distance because the Pt−Pt bond distance results from the average distance of Pt−Pt in Pt_1Sn_1 and Pt−Pt in metallic Pt, while the Pt−Sn bond distance only results from Pt_1Sn_1. The Pt−Sn bond distance of our sample is shorter than that of bulk Pt_1Sn_1, which could be attributed to the microstrain between Pt and Pt_1Sn_1 that influences the Pt−Sn bond distance, as expected for a $Pt@Pt_1Sn_1$ core−shell structure.[16,26]

There are five Pt−Sn alloy phases in the Inorganic Crystal Structure Database (ICSD) with different Pt−Sn compositions, including $PtSn_4$, $PtSn_2$, Pt_2Sn_3, Pt_1Sn_1, and Pt_3Sn (as listed in Table S1). To exclude the possibility of other Pt−Sn phases in our samples, XRD simulations were conducted for these alloys. As shown in Figure S4, the XRD patterns of $PtSn_4$, $PtSn_2$, Pt_2Sn_3, and Pt_1Sn_1 do not match the diffraction peaks of the sample. Although the diffraction peaks of Pt_3Sn are similar to those of Pt, the Pt−Sn bond distance of Pt_3Sn (2.83 Å) is significantly longer than the Pt−Sn bond distance of the sample (2.67 Å from the EXAFS fitting results). Combined with the XRD and EXAFS results, it is concluded that the nanoparticles contain Pt_1Sn_1 and Pt phases. According to the phase diagram, we should obtain numerous types of Pt−Sn alloys by changing the Sn loadings if the structure of the nanoparticles is only controlled by thermodynamics. However, in our Pt−Sn bimetallic catalysts, only the hexagonal Pt_1Sn_1 phase was identified in the nanoparticles, which means that the kinetic diffusion plays an important role to form the structure.[7] In the Pt−Sn bimetallic catalysts, PtO_x on SiO_2 was first reduced to metallic Pt nanoparticles, and then SnO_x was reduced by hydrogen spilled over from Pt at a higher temperature to form surface hexagonal Pt_1Sn_1. The Pt−Sn

https://dx.doi.org/10.1021/acsami.0c05043
ACS Appl. Mater. Interfaces 2020, 12, 25903−25909

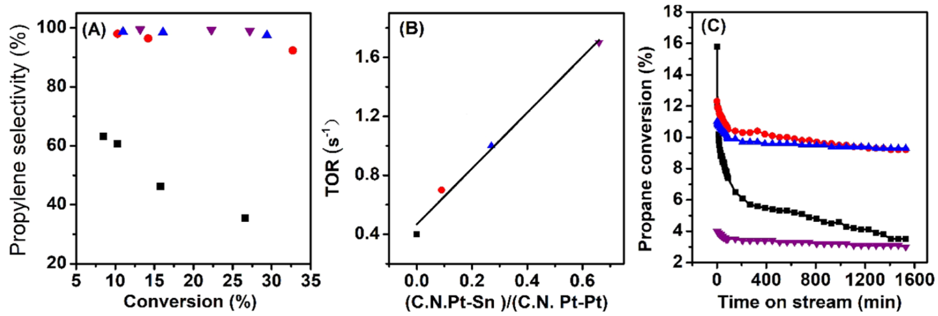

Figure 3. Catalytic performance of the catalysts. (A) Propylene selectivity at different propane conversions. (B) TORs at different Pt−Sn coordination numbers. (C) Stability test of the samples: Pt/SiO_2 (black), $1SnPt/SiO_2$ (red), $4SnPt/SiO_2$ (blue), and $8SnPt/SiO_2$ (purple).

coordination number increases with increasing Sn loadings, which means that the hexagonal Pt_1Sn_1 is not only one surface layer on Pt nanoparticles, instead, the shell thickness of Pt@Pt_1Sn_1 increases with increasing Sn loadings. Notably, the crystal structure of Pt−Sn bimetallic catalysts can be transformed by different supports and preparing methods.[27,28] Vu et al. reported Al_2O_3-supported Pt−Sn catalysts for propane dehydrogenation, which suggested that both Pt_3Sn_1 and Pt_1Sn_1 phases were coexisted in the bimetallic catalysts.[27] Ramachandran et al. applied an atomic layer deposition method to synthesize Pt−Sn bimetallic nanoparticles supported on SiO_2, and their results suggested that the phase compositions of Pt_3Sn, Pt_1Sn_1, and $PtSn_4$ were controllable by changing the Pt/Sn atomic ratios.[28] To investigate the thermodynamic stability of the surface Pt_1Sn_1, XRD spectra of 550 °C and the room temperature of the samples were compared. As shown in Figure S5, aside from the peak shift caused by thermal-induced lattice expansion, the diffraction patterns of 550 °C were similar to those of the room temperature, indicating that the crystal structure was not destroyed at the high temperature, which plays a key role to determine the structure−function relationship.

These as-synthesized catalysts were further evaluated for light alkane dehydrogenation. Compared with the Pt/SiO_2 catalyst, the Sn/SiO_2 catalyst exhibits a negligible activity for propane dehydrogenation (Table S2). As shown in Figure 3A, the propylene selectivity of Pt/SiO_2 is 64% at 8% propane conversion, but the selectivity decreases to 35% when the conversion increases to 27%. With the formation of surface Pt_1Sn_1, propylene selectivity is higher than 92% for all the Pt−Sn bimetallic catalysts at different Sn loadings even higher propane conversion, ca. 30%. Notably, the Pt−Sn coordination number of $1SnPt/SiO_2$ is only 0.8, and there are excessive Pt−Pt bonds, which means that there is only a small amount of Pt_1Sn_1 intermetallic in the $1SnPt/SiO_2$ sample. In this case, if $1SnPt/SiO_2$ is a simple mixture of Pt nanoparticles and Pt_1Sn_1 intermetallic, the propylene selectivity of $1SnPt/SiO_2$ should be very low. Due to the high propylene selectivity of $1SnPt/SiO_2$, we exclude the possibility of a simple mixture of Pt nanoparticles and Pt_1Sn_1 intermetallic, which further validates the proposed Pt@Pt_1Sn_1 core−shell structure. The Pt−Sn coordination number of Pt@Pt_1Sn_1 nanoparticles has a significant effect on the TORs. As shown in Figure 3B, the TOR of Pt/SiO_2 is 0.4 s^{-1}, and the TOR increases with increasing Pt−Sn coordination number. TOR reaches 1.7 s^{-1} for the $8Sn2Pt/SiO_2$ catalyst, which is 4.3 times higher than that of Pt/SiO_2. We also investigated the stability of these catalysts. As displayed in Figure 3C, propane conversion drops very quickly for Pt/SiO_2, which decreases from 16 to 8% within 80 min. By contrast, the Pt−Sn bimetallic catalysts exhibit a high stability for propane dehydrogenation. Notably, the Pt dispersion decreases at a higher Sn loading, which decreases from 31 to 4% when the Sn loading is 8% (Table S3). By oxidizing the surface of the reduced samples, the Fourier transform magnitudes of the Pt−O scattering path continue to decrease with increasing Sn loadings, which may result from the unalloyed Sn species that cover the surface Pt and reduce the Pt dispersion (Figure S6). Thus, it is of critical importance to balance TORs and Pt dispersion in the Pt−Sn bimetallic catalysts.

From the precisely identified structure of the catalysts, DFT calculations were used to study the adsorption energies of the hydrocarbon species involved in propane dehydrogenation over the Pt and Pt−Sn catalysts. The (111) facet of Pt and the (110) facet of Pt_1Sn_1 were selected for calculations due to their lowest surface energy. Due to the difference in Pt−Sn coordination number/shell thickness, a Pt_1Sn_1 shell on the top of Pt was considered as the core−shell nanoparticle has only one surface layer ($Pt_1Sn_1(110)/Pt(111)$), and a Pt_1Sn_1 full-body intermetallic was considered as the nanoparticle has more than one Pt_1Sn_1 surface layer (Tables S4, S5, Figures S7, S8). It has been suggested that $CH_3CH_2CH_2$, CH_3CHCH_3, CH_3CHCH_2, and CH_3CCH_2 are key intermediates in propane dehydrogenation and the adsorption energies of these intermediates on Pt have a significant effect on the catalytic performance.[23,29] As shown in Figure 4A, compared with Pt(111), $Pt_1Sn_1(110)/Pt(111)$ decreases the adsorption energies by 7.8, 7.8, 11.8, 2.9, and 35.2 for $CH_3CH_2CH_3$, $CH_3CH_2CH_2$, CH_3CHCH_3, CH_3CHCH_2, and CH_3CCH_2,

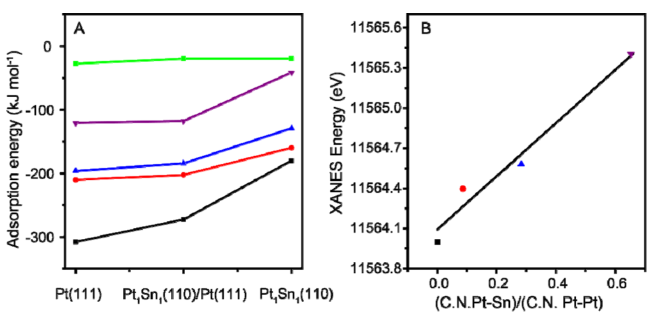

Figure 4. Adsorption energy and XANES energy shift of the catalysts. (A) Adsorption energy of the intermediates on different catalytic surfaces, CH_3CCH_2 (black), $CH_3CH_2CH_2$ (red), CH_3CHCH_3 (blue), CH_3CHCH_2 (purple), and $CH_3CH_2CH_3$ (green). (B) XANES energy shift of the catalysts, Pt/SiO_2 (black), $1SnPt/SiO_2$ (red), $4SnPt/SiO_2$ (blue), and $8SnPt/SiO_2$ (purple).

https://dx.doi.org/10.1021/acsami.0c05043
ACS Appl. Mater. Interfaces 2020, 12, 25903−25909

respectively, whereas the adsorption energies are reduced by 7.8, 50.3, 67, 79.2, and 127.7 for $CH_3CH_2CH_3$, $CH_3CH_2CH_2$, CH_3CHCH_3, CH_3CHCH_2, and CH_3CCH_2, respectively, on $Pt_1Sn_1(110)$. The adsorption energies of all of the investigated adsorbates on $Pt_1Sn_1(110)$ are weaker than those on $Pt_1Sn_1(110)/Pt(111)$, confirming that the Pt−Sn coordination number has an important impact on intermediate adsorption. The electronegativity of Pt is 2.28, while that of Sn is 1.96, which means Sn donates electrons to Pt in Pt_1Sn_1 intermetallic. In the $Pt_1Sn_1(110)/Pt(111)$ model, each surface Pt bonds with three subsurface Pt, which deceases the electronic effects of surface Sn, while surface Pt atoms do not bond with subsurface Pt in the $Pt_1Sn_1(110)$ model. Thus, in our DFT results, the differences in the adsorption energies between Pt(111) and $Pt_1Sn_1(110)/Pt(111)$ are much smaller than those between $Pt_1Sn_1(110)/Pt(111)$ and $Pt_1Sn_1(110)$.

These experiments and theoretical calculations lead to an in-depth understanding of the structure−function relationship. The surface geometric structure of the bimetallic nanoparticles is almost the same (hexagonal Pt_1Sn_1), but the surface electronic structure of these nanoparticles is different, which leads to similar propylene selectivity and different TORs for propane dehydrogenation. The Pt_1Sn_1 phase reduces the Pt−Pt coordination number and Pt ensembles compared with the monometallic Pt catalyst. It has been suggested that Pt threefold hollow sites resulted from large Pt ensembles lead to the formation of alkylidyne species, which is responsible for hydrogenolysis.[30,31] The high propylene selectivity of these Pt−Sn catalysts results from the geometric effects of Sn on Pt that isolate the surface Pt atoms. As shown in Figure 4B, the electronic effects of Sn on Pt lead to a higher level of XANES energy, suggesting a higher level of unfilled Pt 5d states, which reduces the adsorption energies of hydrocarbons on Pt according to the DFT calculations. Since the reaction rates of light alkane dehydrogenation are desorption-limited, lower adsorption energies result in higher TORs of the Pt−Sn bimetallic catalysts.[12] Similar results have been reported in the Pt_1Zn_1 alloys. Resonant inelastic X-ray scattering (RIXS) and DFT results suggest that high TORs of the Pt_1Zn_1 alloys are due to the weakened bonds between Pt and alkenes resulted from the lower energy level of the occupied Pt 5d states and higher energy level of the unoccupied Pt 5d states.[32] Thus, in the Pt−Sn bimetallic catalysts, the high propylene selectivity is due to the geometric effects of Sn on Pt, and the high TORs result from the electronic effects of Sn on Pt.

Solid-supported Pt−Sn bimetallic catalysts are one of the most important catalytic materials for light alkane dehydrogenation. Although Pt−Sn bimetallic catalysts for light alkane dehydrogenation have been studied widely, the intrinsic contribution of Sn on Pt is still under debate. Precisely characterizing and controlling the structure are of critical importance to identify the structure−function relationship. Using regular XRD to determine the structure, many supports, such as Al_2O_3, SAPO-34, ZSM-5, and SBA-15, often produce strong diffraction peaks that cover the potential diffraction peaks of Pt or Pt−Sn alloys with small particle sizes.[33−36] For example, Liu et al. investigated the indium-modified Pt−Sn bimetallic catalysts supported on Al_2O_3 for propane dehydrogenation.[33] In the XRD patterns, only diffraction peaks of Al_2O_3 were observed, while the diffraction peaks of Pt, Sn, and In species were not detected. In this case, the atomic arrangement of the Pt−Sn bimetallic catalysts is still unknown. Another challenge for determining the structure of Pt−Sn alloys is that the structure of Pt_3Sn intermetallic is similar to that of metallic Pt. Deng et al. synthesized a series of Pt−Sn bimetallic catalysts supported on amorphous SiO_2 by a direct reduction method. They proposed that Pt_3Sn was formed at a low Sn loading, while Pt_1Sn_1 was formed when the molar ratio of Sn to Pt reaches 3.[37] Vu et al. reported a Pt−Sn bimetallic catalyst (3% Pt loading 3%, 3% Sn loading) for propane dehydrogenation, which achieved ∼48% propane conversion and ∼90% propylene selectivity at a reaction temperature of 600 °C.[27] They suggested both Pt_3Sn and Pt_1Sn_1 were coexisted in the bimetallic catalysts. In our Pt−Sn bimetallic catalysts, the surface Pt−Sn alloys maintain a hexagonal Pt_1Sn_1 structure with changing Sn loadings. Even though the XRD pattern of Pt_3Sn is very similar to that of $1SnPt/SiO_2$, we exclude the possibility of Pt_3Sn in our bimetallic samples by comparing the Pt−Sn bond distance of our samples and Pt_3Sn intermetallic. Combined with experiments and theoretical calculations, we reveal the geometric and electronic effects of Sn on Pt for propane dehydrogenations. This work highlights the importance of precisely characterizing and the controlling catalytic surface structure of small nanoalloys in heterogeneous catalysis.

4. CONCLUSIONS

In summary, a series of 2−3 nm $Pt@Pt_1Sn_1$ nanoparticles with a highly ordered hexagonal Pt_1Sn_1 intermetallic shell on Pt nanoparticles were identified by in situ synchrotron XRD and XAFS. Compared with the monometallic Pt catalyst, Pt−Sn bimetallic catalysts exhibit higher TORs, propylene selectivity, and stability for propane dehydrogenation. At the same time, TORs increase with increasing Pt−Sn coordination number, whereas propylene selectivity is not significantly influenced by the Pt−Sn coordination number. The high propylene selectivity of the Pt−Sn alloys is attributed to the geometric effects of Sn that reduce the Pt ensembles, and the high TORs are due to the electronic effects that weaken Pt−hydrocarbon chemisorption energies. This work highlights the importance of precisely characterizing and controlling the catalytic surface structure of small nanoalloys in heterogeneous catalysis.

■ ASSOCIATED CONTENT

Supporting Information

The Supporting Information is available free of charge at https://pubs.acs.org/doi/10.1021/acsami.0c05043.

> Detailed experimental section, STEM images of the catalysts, *R* space, and *k* space EXAFS fitting results, structure of Pt−Sn alloys from ICSD, XRD simulations of Pt−Sn alloys, XRD patterns at different temperatures, catalytic performance of Pt/SiO_2 and Sn/SiO_2, Pt dispersion determined by CO chemisorption, *R* space EXAFS of the oxidized samples, calculated surface energies of Pt_1Sn_1, adsorption energies for the most stable adsorption configurations, surface morphology and corresponding adsorption sites, and visual structure of most stable adsorption configurations (PDF)

■ AUTHOR INFORMATION

Corresponding Authors

Miaolun Jiao − *School of Chemical Engineering and Technology, Tianjin University, Tianjin 300072, China;* orcid.org/0000-0001-6662-659X; Email: jiaomiaolun@tju.edu.cn

https://dx.doi.org/10.1021/acsami.0c05043
ACS Appl. Mater. Interfaces 2020, 12, 25903−25909

Jeffrey T. Miller − *Davidson School of Chemical Engineering, Purdue University, West Lafayette, Indiana 47907, United States;* orcid.org/0000-0002-6269-0620; Email: mill1194@purdue.edu

Authors

Chenliang Ye − *Department of Chemistry, Tsinghua University, Beijing 100084, China; Davidson School of Chemical Engineering, Purdue University, West Lafayette, Indiana 47907, United States; School of Chemical Engineering and Technology, Tianjin University, Tianjin 300072, China*

Mao Peng − *School of Chemical Engineering and Technology, Tianjin University, Tianjin 300072, China*

Yunhao Wang − *School of Chemical Engineering and Technology, Tianjin University, Tianjin 300072, China*

Ningqiang Zhang − *Department of Chemistry, Tsinghua University, Beijing 100084, China*

Dingsheng Wang − *Department of Chemistry, Tsinghua University, Beijing 100084, China;* orcid.org/0000-0003-0074-7633

Complete contact information is available at: https://pubs.acs.org/10.1021/acsami.0c05043

Author Contributions

‖C.Y. and M.P. contributed equally to this work.

Notes

The authors declare no competing financial interest.

ACKNOWLEDGMENTS

This paper is based upon the work supported by the National Science Foundation under Cooperative Agreement No. EEC-1647722. MRCAT operations, beamline 10-BM, are supported by the Department of Energy and the MRCAT member institutions. The authors also acknowledge the use of beamline 11-ID-C at APS. C.Y. thanks the financial support from the Chinese Scholarship Council (CSC).

REFERENCES

(1) Cai, S.; Duan, H.; Rong, H.; Wang, D.; Li, L.; He, W.; Li, Y. Highly Active and Selective Catalysis of Bimetallic Rh_3Ni_1 Nanoparticles in the Hydrogenation of Nitroarenes. *ACS Catal.* **2013**, *3*, 608−612.

(2) Gallagher, J. R.; Childers, D. J.; Zhao, H.; Winans, R. E.; Meyer, R. J.; Miller, J. T. Structural Evolution of an Intermetallic Pd−Zn Catalyst Selective for Propane Dehydrogenation. *Phys. Chem. Chem. Phys.* **2015**, *17*, 28144−28153.

(3) Zhang, X.; Liu, Y. X.; Deng, J. G.; Yu, X. H.; Han, Z.; Zhang, K. F.; Dai, H. X. Alloying of Gold with Palladium: An Effective Strategy to Improve Catalytic Stability and Chlorine-tolerance of the 3DOM CeO_2-supported Catalysts in Trichloroethylene Combustion. *Appl. Catal., B* **2019**, *257*, 117879−117890.

(4) Nutt, M. O.; Heck, K. N.; Alvarez, P.; Wong, M. S. Improved Pd-on-Au Bimetallic Nanoparticle Catalysts for Aqueous-phase Trichloroethene Hydrodechlorination. *Appl. Catal., B* **2006**, *69*, 115−125.

(5) Tew, M. W.; Emerich, H.; van Bokhoven, J. A. Formation and Characterization of PdZn Alloy: A Very Selective Catalyst for Alkyne Semihydrogenation. *J. Phys. Chem. C* **2011**, *115*, 8457−8465.

(6) Furukawa, S.; Komatsu, T. Intermetallic Compounds: Promising Inorganic Materials for Well-structured and Electronically Modified Reaction Environments for Efficient Catalysis. *ACS Catal.* **2017**, *7*, 735−765.

(7) Wu, Z.; Wegener, E. C.; Tseng, H.-T.; Gallagher, J. R.; Harris, J. W.; Diaz, R. E.; Ren, Y.; Ribeiro, F. H.; Miller, J. T. Pd−In Intermetallic Alloy Nanoparticles: Highly Selective Ethane Dehydrogenation Catalysts. *Catal. Sci. Technol.* **2016**, *6*, 6965−6976.

(8) Wu, Z.; Bukowski, B. C.; Li, Z.; Milligan, C.; Zhou, L.; Ma, T.; Wu, Y.; Ren, Y.; Ribeiro, F. H.; Delgass, W. N. Changes in Catalytic and Adsorptive Properties of 2 nm Pt_3Mn Nanoparticles by Subsurface Atoms. *J. Am. Chem. Soc.* **2018**, *140*, 14870−14877.

(9) Cesar, L. G.; Yang, C.; Lu, Z.; Ren, Y.; Zhang, G. H.; Miller, J. T. Identification of a Pt_3Co Surface Intermetallic Alloy in Pt-Co Propane Dehydrogenation Catalysts. *ACS Catal.* **2019**, *9*, 5231−5244.

(10) LiBretto, N. J.; Yang, C.; Ren, Y.; Zhang, G. H.; Miller, J. T. Identification of Surface Structures in Pt_3Cr Intermetallic Nanocatalysts. *Chem. Mater.* **2019**, *31*, 1597−1609.

(11) Siirola, J. J. The Impact of Shale Gas in the Chemical Industry. *AIChE J.* **2014**, *60*, 810−819.

(12) Sattler, J. J. H. B.; Javier, R. M.; Eduardo, S. J.; Weckhuysen, B. M. Catalytic Dehydrogenation of Light Alkanes on Metals and Metal oxides. *Chem. Rev.* **2014**, *114*, 10613−10653.

(13) Zhang, Y.; Zhou, Y.; Qiu, A.; Wang, Y.; Xu, Y.; Wu, P. Propane Dehydrogenation on PtSn/ZSM-5 Catalyst: Effect of Tin as a Promoter. *Catal. Commun.* **2006**, *7*, 860−866.

(14) Vu, B. K.; Song, M. B.; Ahn, I. Y.; Suh, Y.-W.; Suh, D. J.; Kim, W.-I.; Koh, H.-L.; Choi, Y. G.; Shin, E. W. Pt−Sn Alloy Phases and Coke Mobility over Pt−Sn/Al2O3 and Pt−Sn/$ZnAl_2O_4$ Catalysts for Propane Dehydrogenation. *Appl. Catal., A* **2011**, *400*, 25−33.

(15) Serrano-Ruiz, J. C.; Huber, G. W.; Sánchez-Castillo, M. A.; Dumesic, J. A.; Rodríguez-Reinoso, F.; Sepúlveda-Escribano, A. Effect of Sn Addition to Pt/CeO_2−Al_2O_3 and Pt/Al_2O_3 Catalysts: An XPS, Sn-199 Mossbauer and Microcalorimetry Study. *J. Catal.* **2006**, *241*, 378−388.

(16) Ye, C.; Wu, Z.; Liu, W.; Ren, Y.; Zhang, G.; Miller, J. T. Structure Determination of a Surface Tetragonal Pt_1Sb_1 Phase on Pt Nanoparticles. *Chem. Mater.* **2018**, *30*, 4503−4507.

(17) Li, J.; Li, J.; Zhao, Z.; Fan, X.; Liu, J.; Wei, Y.; Duan, A.; Xie, Z.; Liu, Q. Size Effect of TS-1 Supports on the Catalytic Performance of PtSn/TS-1 Catalysts for Propane Dehydrogenation. *J. Catal.* **2017**, *352*, 361−370.

(18) Camacho-Bunquin, J.; Ferrandon, M. S.; Sohn, H.; Kropf, A. J.; Yang, C.; Wen, J. G.; Hackler, R. A.; Liu, C.; Celik, G.; Marshall, C. L.; Stair, P. C.; Delferro, M. Atomically Precise Strategy to a PtZn Alloy Nanocluster Catalyst for the Deep Dehydrogenation of n-Butane to 1,3-Butadiene. *J. Catal.* **2018**, *8*, 10058−10063.

(19) Wegener, E. C.; Wu, Z. W.; Tseng, H. T.; Gallagher, J. R.; Ren, Y.; Diaz, R. E.; Ribeiro, F. H.; Miller, J. T. Structure and Reactivity of Pt-In Intermetallic Alloy Nanoparticles: Highly Selective Catalysts for Ethane Dehydrogenation. *Catal. Today* **2018**, *299*, 146−153.

(20) Sun, G. D.; Zhao, Z. J.; Mu, R. T.; Zha, S. J.; Li, L. L.; Chen, S.; Zang, K. T.; Luo, J.; Li, Z. L.; Purdy, S. C.; Kropf, A. J.; Miller, J. T.; Zeng, L.; Gong, J. L. Breaking the Scaling Relationship via Thermally Stable Pt/Cu Single Atom Alloys for Catalytic Dehydrogenation. *Nat. Commun.* **2018**, *9*, No. 4454.

(21) Wu, J.; Peng, Z.; Bell, A. T. Effects of Composition and Metal Particle Size on Ethane Dehydrogenation over Pt_xSn_{100-x}/Mg(Al)O ($70 \leqslant x \leqslant 100$). *J. Catal.* **2014**, *311*, 161−168.

(22) Cortright, R. D.; Hill, J. M.; Dumesic, J. A. Selective Dehydrogenation of Isobutane over Supported Pt/Sn Catalysts. *Catal. Today* **2000**, *55*, 213−223.

(23) Yang, M.-L.; Zhu, Y.-A.; Zhou, X.-G.; Sui, Z.-J.; Chen, D. First-Principles Calculations of Propane Dehydrogenation over PtSn Catalysts. *ACS Catal.* **2012**, *2*, 1247−1258.

(24) Wong, A.; Liu, Q.; Griffin, S.; Nicholls, A.; Regalbuto, J. Synthesis of Ultrasmall, Homogeneously Alloyed, Bimetallic Nanoparticles on Silica Supports. *Science* **2017**, *358*, 1427−1430.

(25) Gallagher, J. R.; Li, T.; Zhao, H.; Liu, J.; Lei, Y.; Zhang, X.; Ren, Y.; Elam, J. W.; Meyer, R. J.; Winans, R. E.; Miller, J. T. In situ Diffraction of Highly Dispersed Supported Platinum Nanoparticles. *Catal. Sci. Technol.* **2014**, *4*, 3053−3063.

(26) Feng, Q.; Zhao, S.; He, D.; Tian, S.; Gu, L.; Wen, X.; Chen, C.; Peng, Q.; Wang, D.; Li, Y. Strain Engineering to Enhance the Electrooxidation Performance of Atomic-Layer Pt on Intermetallic Pt3Ga. *J. Am. Chem. Soc.* **2018**, *140*, 2773−2776.

(27) Vu, B. K.; Song, M. B.; Ahn, I. Y.; Suh, Y.-W.; Suh, D. J.; Kim, W.-I.; Koh, H.-L.; Choi, Y. G.; Shin, E. W. Propane Dehydrogenation over Pt−Sn/Rare-earth-doped Al_2O_3: Influence of La, Ce, or Y on the Formation and Stability of Pt−Sn Alloys. *Catal. Today* **2011**, *164*, 214−220.

(28) Ramachandran, R. K.; Filez, M.; Dendooven, J.; Galvita, V. V.; Poelman, H.; Solano, E.; Fonda, E.; Marin, G. B.; Detavernier, C. Size- and Composition-controlled Pt−Sn Bimetallic Nanoparticles Prepared by Atomic Layer Deposition. *RSC Adv.* **2017**, *7*, 20201−20205.

(29) Nykänen, L.; Honkala, K. Selectivity in Propene Dehydrogenation on Pt and Pt_3Sn Surfaces from First Principles. *ACS Catal.* **2013**, *3*, 3026−3030.

(30) Tsai, Y.-L.; Koel, B. E. Temperature-Programmed Desorption Investigation of the Adsorption and Reaction of Butene Isomers on Pt (111) and Ordered Pt− Sn Surface Alloys. *J. Phys. Chem. B* **1997**, *101*, 2895−2906.

(31) Nomikou, Z.; Van Hove, M.; Somorjai, G. Molecular Modeling of Ethylidyne Adsorption and Diffusion on Pt (111). *Langmuir* **1996**, *12*, 1251−1256.

(32) Cybulskis, V. J.; Bukowski, B. C.; Tseng, H.-T.; Gallagher, J. R.; Wu, Z.; Wegener, E.; Kropf, A. J.; Ravel, B.; Ribeiro, F. H.; Greeley, J.; Miller, J. T. Zinc Promotion of Platinum for Catalytic Light Alkane Dehydrogenation: Insights into Geometric and Electronic Effects. *ACS Catal.* **2017**, *7*, 4173−4181.

(33) Liu, X.; Lang, W. Z.; Long, L. L.; Hu, C. L.; Chu, L. F.; Guo, Y. J. Improved Catalytic Performance in Propane Dehydrogenation of PtSn/gamma-Al_2O_3 Catalysts by Doping Indium. *Chem. Eng. J.* **2014**, *247*, 183−192.

(34) Nawaz, Z.; Wei, F. Hydrothermal Study of Pt-Sn-based SAPO-34 Supported Novel Catalyst Used for Selective Propane Dehydrogenation to Propylene. *J. Ind. Eng. Chem.* **2010**, *16*, 774−784.

(35) Zhang, Y. W.; Zhou, Y. M.; Zhang, S. B.; Zhou, S. J.; Sheng, X. L.; Wang, Q. L.; Zhang, C. Catalytic Structure and Reaction Performance of PtSnK/ZSM-5 Catalyst for Propane Dehydrogenation: Influence of Impregnation Strategy. *J. Mater. Sci.* **2015**, *50*, 6457−6468.

(36) Santhosh Kumar, M.; Chen, D.; Holmen, A.; Walmsley, J. C. Dehydrogenation of Propane over Pt-SBA-15 and Pt-Sn-SBA-15: Effect of Sn on the Dispersion of Pt and Catalytic Behavior. *Catal. Today* **2009**, *142*, 17−23.

(37) Deng, L. D.; Miura, H.; Shishido, T.; Hosokawa, S.; Teramura, K.; Tanaka, T. Dehydrogenation of Propane over Silica-Supported Platinum-Tin Catalysts Prepared by Direct Reduction: Effects of Tin/Platinum Ratio and Reduction Temperature. *ChemCatChem* **2014**, *6*, 2680−2691.

https://dx.doi.org/10.1021/acsami.0c05043
ACS Appl. Mater. Interfaces 2020, 12, 25903−25909